PAPER • **OPEN ACCESS**

Hydrography and turbulent mixing in the Banda Sea inferred from Argo profiles

To cite this article: A Purwandana *et al* 2023 *IOP Conf. Ser.: Earth Environ. Sci.* **1251** 012007

View the article online for updates and enhancements.

You may also like

- The importance of the Banda Sea for tuna conservation area: A review of studies on the biology and the ecology of tuna
W N Satrioajie, Suyadi, A Syahailatua et al.

- The Thermocline Layer and Chlorophyll-a Concentration Variability during Southeast Monsoon in the Banda Sea
Nikita Pusparini, Budi Prasetyo, Ambariyanto et al.

- Circulation dynamics of the Banda Sea estimated from argo profiles
M F A Ismail, A Taofiqurohman and A Purwandana

245th ECS Meeting • May 26-30, 2024 • San Francisco, CA

Submit now!

Don't miss your chance to present!

Connect with the leading electrochemical and solid-state science network!

Deadline Extended: December 15, 2023

This content was downloaded from IP address 212.201.152.38 on 11/12/2023 at 14:47

Hydrography and turbulent mixing in the Banda Sea inferred from Argo profiles

A Purwandana[1*], M F A Ismail[2,3], D Nugroho[1], A S Atmadipoera[4], I Kampono[1]

[1] Research Center for Oceanography-National Research and Innovation Agency (RCO-BRIN), Jakarta, Indonesia
[2] Research Center for Climate and Atmosphere-National Research and Innovation Agency (PRIMA-BRIN), Bandung, Indonesia
[3] GEOMAR Helmholtz-zentrum fur Ozeanforschung, Kiel, Germany
[4] Faculty of Fisheries and Marine Sciences, IPB University, Bogor, Indonesia

*E-mail : adip003@brin.go.id

Abstract. Two Argo floats circulating in the Banda Sea from July 2017 until April 2019 were analysed to inspect the hydrography and vertical mixing properties. The maximum intrusion of Pacific thermocline and intermediate layers in the Banda Sea were identified during the Southeast Monsoon period with high temporal variability in the mixed layer (<100 m), where fresher and warmer waters are maximum during the transition season, from Northwest to Southeast Monsoon months. The monsoonal variability was also featured by the signature of downwelling and upwelling events, respectively. The upwelling rate of the colder water, isotherm 27° C, from 100 m to 10 m depth is ~0.7 m day^{-1}, from March to June 2018. The thickening of mixed layer occurred during the Northwest Monsoon months. The monsoonal gyre exists in the Banda Sea as shown by Argo floats trajectory. The highest rate of turbulent kinetic energy dissipation and vertical diffusivity of >10^{-8} m^2 s^{-3} and [10^{-5}–10^{-4}] m^2 s^{-1}, respectively, were observed in the mixed layer and thermocline layer, with the decreasing trend deeper. The dissipation rate and diffusivity are comparable to previous direct estimates and models, suggesting the potential use of Argo float datasets to quantify vertical mixing in the future.

Keywords: Argo float, ITF, Indonesian seas, vertical mixing, Banda Sea, Thorpe method

1. Introduction

The Indonesian seas connects the Pacific and the Indian Oceans via the Indonesian throughflow (ITF). The ITF significantly contributes to oceanic circulations globally, as it is part of the thermohaline circulation, which supplies warm and low salinity anomaly to the Indian Ocean which then exporting poleward via the Agulhas current [1]–[3]. In addition, the ITF is exposed to strong mixing in the Indonesian seas, resulting lower sea surface temperature anomaly, which impacts to the atmospheric processes [4].

Previous studies indicated that the Indonesian waters had been influenced by North and South Pacific sources via ITF, which can be characterized easily from their signatures in the thermocline and intermediate layers. The North Pacific Subtropical Water (NPSW) and South Pacific Subtropical Water (SPSW) laid in the thermocline layer while the North Pacific Intermediate Water (NPIW) and South Pacific Intermediate Water (SPIW) laid in the intermediate layer [5]–[8]. The Pacific

Content from this work may be used under the terms of the Creative Commons Attribution 3.0 licence. Any further distribution of this work must maintain attribution to the author(s) and the title of the work, journal citation and DOI.
Published under licence by IOP Publishing Ltd

thermocline (NPSW/SPSW) and intermediate layers (NPIW/SPIW) are centered in the isopycnal σ_θ = 24–24.5 and σ_θ = 25–26.5, respectively, with maximum salinity, S_{max} [34.5–35 psu] and minimum salinity S_{min} [34.2–34.5 psu], respectively [9], [10]. The formation of the ITF in the Indonesian seas is well documented by the previous study [3].

The North Pacific water masses enter the Indonesian seas via the western route of the ITF [1], [11], while the South Pacific water masses enter the Indonesian seas via the eastern route [1], [2]. The western route allows the North Pacific water masses enter the Mindanao Strait, Sulawesi Sea and Makassar Strait, and then flow out to the Indian Ocean through the Lombok Strait, the Banda Sea, and the Timor Sea. The eastern route allows the South Pacific water masses enter the Halmahera Sea, a portion enters the Maluku Sea, and the remaining penetrates the Seram and enters the Banda Sea. Note that a recent study evidenced that in the upper layer, the ITF via the Halmahera Sea varies seasonally, i.e. maximum throughflow during Southeast Monsoon (SEM, from June to November) and low during Northwest Monsoon (NWM, from December to May) [2], [12]. The Pacific water masses converge in the Banda Sea.

Early studies in the Banda Sea showed that during NWM period, the intermediate Pacific water masses become fresher due to mixing with local water masses from the Java Sea and Makassar Strait [13]. It was revealed that above 500 m layer, the southern part Banda Sea water mass is younger than the northern part due to being directly fed by the Flores Sea while in the deeper layer, the northern Banda Sea water mass is younger than the southern part as it is fed by the flow from the Seram and the Halmahera Seas [14]. A strong deeper layer throughflow via Lifamatola Passage supplies the deeper layer (lower thermocline and intermediate layer) of the Banda Sea by the South Pacific water masses [15].

The Banda Sea is a semi-enclosed seas featured by a west-facing C-shape, the Banda Arc/The Webber Deep. The map of the Banda Sea is shown in Figure 1a. The Banda Sea is directly connected to the Flores Sea in the western side and to the Maluku and Halmahera Seas in the northern sides, and the Timor Sea in the southern side. The eastern section of the Banda Sea within the rectangular region from 4°–7° S and 129°–132° E (the locus of this study) is bordered by the shelf break of the Maluku Islands, Aru Islands, Barat Daya Islands, and Tanimbar Islands.

Early observations reported that the Banda Sea stratification and circulation are forced by the seasonally reversing monsoon winds, which potentially influence the ITF water masses [5], [16]. It was hypothesized that during the NWM, the surface water from the Flores Sea either sinks in the Banda Sea or is exported from the Banda Sea to the Halmahera and Maluku Seas. A combination of water mass analysis and models in the Banda Sea found that the intermediate Pacific water masses have become fresher due to mixing with the water masses from the Java Sea and Makassar Strait in the Northwest monsoon [13]. In addition, it was suggested that the Banda Sea appears to be flushed from the Pacific water masses with a typical flushing time of 40 years [13], [17].

The Banda Sea is exposed to seasonal upwelling/downwelling, driven by wind-stress curl over the Banda Sea. The upwelling event is also a compensating effect of the Timor Current which takes the water out of the eastern Banda Sea during the SEM period [18]. The Ekman upwelling is maximum in May and June. The average Ekman upwelling velocity is 2.36×10^{-6} m s^{-1} (1.27 Sv) from April to December, and Ekman downwelling is maximum in February at 1.0 Sv. They found the mean Ekman pumping is about 0.75 Sv (1 Sv = 1×10^6 m^3 s^{-1}) upwelling.

The Banda Sea characteristics largely differ from the Pacific water masses [14]. Quantifying the dissipation rate and mixing in a lack of observations region in the Indonesian waters, i.e., the Banda Sea, is important from the perspective of water masses transformation. How the Banda Sea is influenced by the Pacific water masses and what drives the formation of the Banda Sea water masses have yet to be discovered. Several studies suggested that internal tides are responsible for the intense mixing mainly occurring in narrow passages [19]–[22]. The vertical mixing in the central Banda Sea is weak [23], [24]. Understanding the mechanisms working in the Banda Sea is also interesting to get a better insight into the ITF water masses transformation models since most of them neglect local stratifications [25]–[27], reducing their validity. The existence of seasonal upwelling-downwelling

events should not be neglected in this case since enhanced atmospheric driven mixing can strengthen the upwelling (e.g., a cooling mechanism). This study aims to reveal the spatiotemporal variability of water masses, physical mechanisms working in the Banda Sea, and estimate turbulent kinetic energy (TKE) dissipation rates and vertical diffusivity which may be less responsible for the Banda water masses formation as has been indicated by numerous studies.

The paper is organized as follows. Section 2 introduces the dataset and the methods used to characterize the hydrography and to estimate the TKE dissipation rate and vertical diffusivity from observations. Results are presented in Section 3: the hydrography is described in Subsection 3.1. subsection 3.2 focuses on the characterization of dissipation and mixing. Subsection 3.3 focuses on the comparison between observations and regional models of the dissipation rates and vertical diffusivity. Conclusions are drawn in Section 4.

2. Methods

Argo profiles in the Banda Sea, i.e. Platform/ID 6901746/289311 (July 29th, 2017 to October 18th, 2018) and Platform/ID 6901747/360575 (September 7th, 2018 to April 7th, 2019) acquired from the Argo profiles center [28] were analyzed to investigate spatiotemporal variability of the water masses and to infer TKE dissipation rates from their temperature and salinity profiles. A total of 252 vertical casts were used in this study. The Argo profiling cycle comprises four stages: ascending, surface drifting, diving, and deep drifting. The temperature and salinity profiles are measured during the ascending period. The Argo drifts on the surface for about 7–25 h to transmit data to ground stations via satellites.

Typically, the temperatures and pressures in the Argo profiles have an accuracy of up to ±0.002°C and ±2.4 dbar, respectively. However, the salinity has accuracy only up to ±0.01 psu [29]. Vertically, the Argo float has different resolution sampling. Since they have vertically irregular vertical spacing, we re-sampled the vertical spacing into the regular base at 1 dbar (~1 m) resolution. We exclude the upper 10 m, which are strongly possibly impacted by instrument heaving by surface waves, leading to spurious overturns due to temperature and conductivity (~salinity) sensors mismatch. The horizontal spatiotemporal trajectory of the Argo is shown in Figure 1b.

The Advanced Scatterometer (ASCAT) wind data by Remote Sensing Systems and sponsored by NASA [30] with a spatial resolution of 25 km was extracted daily for the region and period of Argo circulating in the Banda Sea (129.5^{o}–131.5^{o} E; 4°–6° S) to track seasonal variability related to monsoon as well as to cross-validate upwelling-downwelling events.

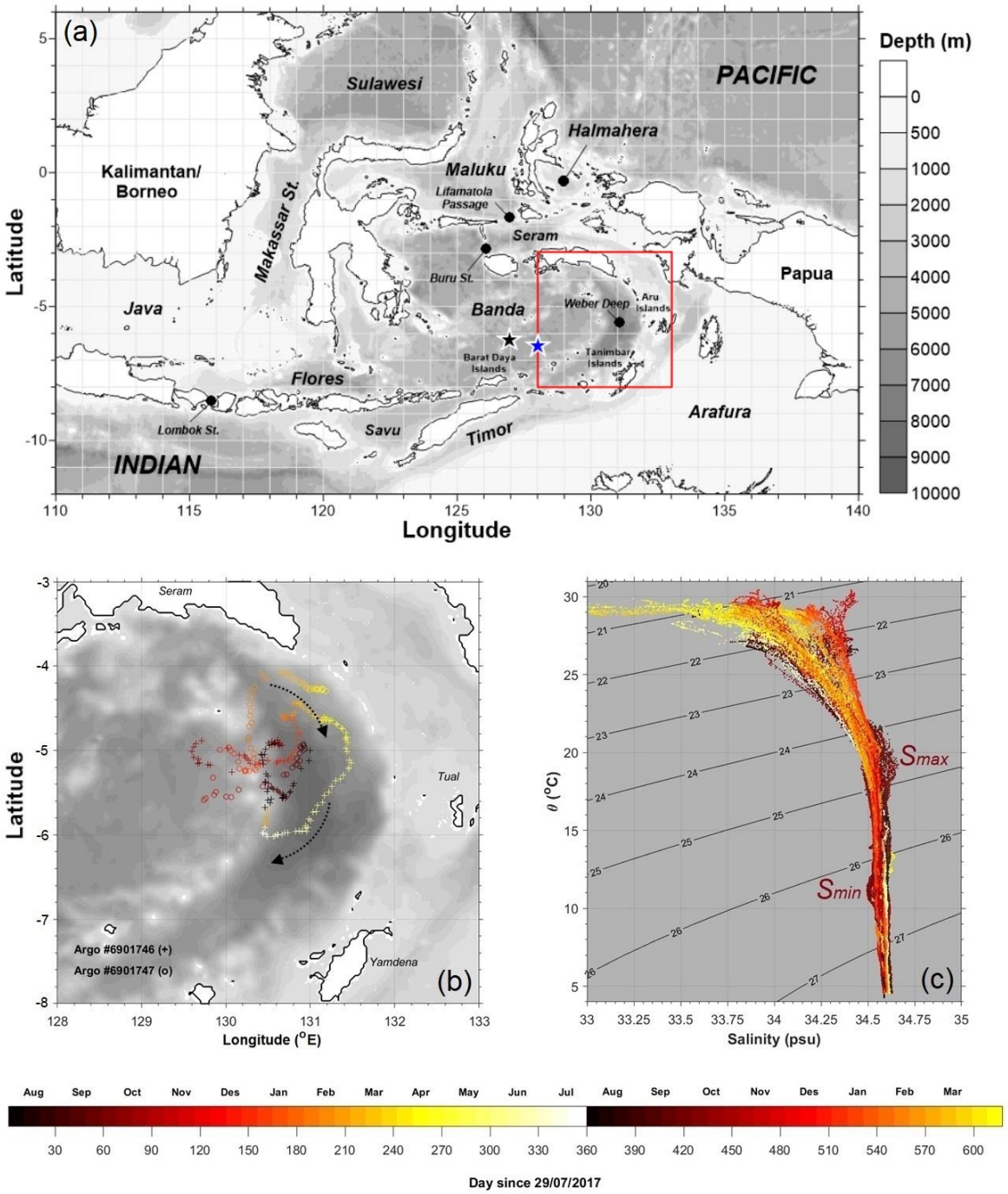

Figure 1. (a) Map of Indonesian seas with basins, straits, and channels labelled. The red box is the central and eastern Banda Sea area, enlarged in (b), and the black and blue stars are the Indonesian Mixing Project (INDOMIX) 2010 station and the ARLINDO Microstructure Experiment (ARMIX) 1999 station, respectively. The topography from ETOPO is shown in the background. (b) Track of two Argo floats in the Banda Sea, i.e., Platform #6901746 (plus symbol) and Platform #6901747 (circle symbol) with color-changing refer to temporal dynamics. The dashed arrows are the schematic current direction inferred from the Argo's trajectory and represent the general circulation pattern indicated by previous studies [31], [32]. (c) Temperature-Salinity diagram with color-changing refers to temporal dynamics. Salinity maximum (S_{max}) and salinity minimum (S_{min}) are the typical Pacific thermocline and intermediate layers, respectively.

2.1. Mixing estimates

Two sets of Argo floats circulating in the Banda Sea from July 2017 to April 2019 are available to map the hydrography and TKE dissipation rates in this region. Different methods and datasets have been used by previous studies [33]–[35]. The temperature and salinity profiles gained from observations are often used to quantify the diapycnal mixing properties [36]–[38]. Here, the mixing properties from Argo profiles are quantified using an improved Thorpe method [39]. The TKE dissipation rate is estimated as,

$$\varepsilon_{\text{Th-GM}} = \begin{cases} 0.64 L_{\text{T}}^2 N^3, & \text{when there is overturn} \\ \max\left(1\times10^{-10}, \varepsilon_0\left(\dfrac{N^2}{N_0^2}\right)\right), & \text{when no overturn observed} \end{cases} \tag{1}$$

Thorpe length, L_{T} is rms value of vertical displacement of unstable water mass parcel to get stable gravitationally, N is buoyancy frequency, 1×10^{-10} is the lowest dissipation rate ever observed using microstructure profiler in the Banda Sea [21], [24]; $\varepsilon_0 = 7\times10^{-10}$ m^2 s^{-3} and $N_0 = 3$ cph are the Garrett and Munk dissipation rate [40] and respected buoyancy frequency. Different from that of the classical Thorpe method, this improved method sets the dissipation rate values at the portion of profiles when no overturns observed with a background dissipation rate of *max* (1×10^{-10} m^2 s^{-3}, $\varepsilon_0(N^2/N_0^2)$), hence the final dissipation rate, termed as $\varepsilon_{\text{Th-GM}}$, produces the continuous profile.

Since the original measured Argo profile has an irregular vertical resolution, i.e., higher resolution in the upper profile and lower resolution in the deeper profile, we re-sampled the profile by interpolating at 1 m resolution. We realize that fewer overturns will be observed in the deeper profile due to lower vertical resolution in the deeper layer than in the upper layer. Yet, in the Banda Sea, this limitation will be compensated by the fact that there is a lack of turbulent events as has been confirmed by previous studies [21], [22], [39]. We considered the use of this improved Thorpe method by inspecting the profile trend of the TKE dissipation rate from direct measurements and models in the Banda Sea carefully [22], [24]–[26] before eventually deciding to use it. Note that this method does not consider only the turbulent patch (Thorpe displacement) but also the GM dissipation rate which was proven comparable to the direct method in the far-field region [21], [39]. Indeed, the method will be valid in relatively calm waters/open seas when a few numbers of overturn is observed. Using our method, such a condition will set the dissipation rate into its background value. This method was also built by assuming that the energy dissipation rate triggered by internal wave interactions leading to turbulence, mainly in the deeper layer. Once the dissipation rate is estimated, the vertical diffusivity is calculated as:

$$K_{\rho\,\text{Th-GM}} = \Gamma \frac{\varepsilon_{\text{Th-GM}}}{N^2} \tag{2}$$

where Γ, the mixing efficiency, $\Gamma = 0.2$ [41]. The spatial variability of hydrography and TKE dissipation rates are built by gridding spatially over 0.1° space and by vertical averaging at depth intervals of 50–300 m, 300–500 m, 500–800 m, 800–1000 m; representing the upper thermocline, lower thermocline, intermediate layer, and deeper layer, respectively; and also density class layers, i.e. σ_θ = 21–22, 22–23, 23–24, 24–25, 25–26 and 26–27 kg m^{-3}, to focus on typical of the water masses.

We compare our mean vertical profile of the TKE dissipation rate and vertical diffusivity inferred using the Thorpe scale method with vertical microstructure profiler (VMP) from INDOMIX 2010 (126.9980° E; 6.2855° S) and ARMIX 1999 (128° E; 6.5° S) in the central Banda Sea. The station positions are shown in Figure 7a. In addition, we also compare our dissipation rate with the product of 1/100° horizontal resolution 3D hydrostatic MITGC model by Nagai and Hibiya [25], hereinafter NAG15 and the 1/12° horizontal resolution 3D hydrostatic model NEMO 2.3 by Nugroho et al. [26], hereinafter NUG18; at INDOMIX 2010 stations.

2.2. Ekman pumping velocity

The vertical Ekman pumping velocity, w_E (m s^{-1}), is estimated from the curl of the surface wind stress using the equation [42]

$$w_E = \frac{1}{\rho_w f}\left(\frac{\partial \tau_y}{\partial x} - \frac{\partial \tau_x}{\partial y}\right) \tag{3}$$

ρ_w is seawater density (1025 kg m^{-3}), f is the Coriolis parameter, τ_y and τ_x are the meridional and zonal components of surface wind stress, respectively. The methods used to compute the surface wind stress are described by a previous study [43]. Positive and negative values of w_E are considered favorable for upwelling and downwelling conditions, respectively. This study constructed the vertical Ekman velocity using Climate Data Toolbox for MATLAB from [44].

3. Results and Discussion

3.1. Hydrography

The Argo floats circulated almost locally within a 2°×2° radius in the Banda Sea for nearly two years. The trajectory period of the floats is shown in Figure 1b. Previous studies estimated the Argo floats horizontal velocity using a constant shear yet only resulted in limited success [45]. Therefore, we do not spend more effort to estimate the mean velocity in this study further. Roughly, the path of the float's trajectory indicated a persistent eastern boundary current in the Banda Sea during the NWM period, flowing from the northwestern Banda Sea towards the eastern part and then deflected southward following the contour of the Webber Deep. A relatively low radius of the circulation of the float indicates the existence of seasonal gyre in the Banda Sea, probably driven by monsoonal winds. Such indication is likely in accordance to previous simulation study which stated that the Banda Sea has anticyclonic circulations in the upper 500 m layer and cyclonic circulations below [46], [47].

The Banda Sea has a typical water masses characteristic that is mainly different from North or South Pacific water masses. Our datasets indicate a minor influence of Pacific water masses, as shown in Figure 1c. The Pacific thermocline and intermediate water masses signatures, i.e., S_{max} and S_{min}, respectively existed during the SEM period from August to November (darker plots); and no more Pacific water masses traces remained during NWM months (brighter plots). This finding strengthens previous studies that suggested maximum Pacific intrusion during the SEM period [48]. We also found an intensive fresh waters layer < 33.75 psu in the upper layer (σ_θ < 22) which is maximum during NWM months. Figure 2 shows the map of salinity mean for a given density range to investigate its spatial variability. The mixed layer (σ_θ = 21–23) is characterized by low salinity, <34.4 psu; the upper thermocline layer (σ_θ = 23-24) is characterized by salinity 34.3–35.5 psu; the core layer of the thermocline (σ_θ = 24–25) is characterized by medium to high salinity 34.4–34.6 psu; the intermediate and deeper layer (σ_θ>25) are characterized by higher salinity > 34.5 psu.

We suggest that low salinity (< 34 psu) in the upper 100 m (the mixed layer) during NWM period, with maximum intensity in April (Figure 3c), is a contribution from the western Banda Sea which contains freshwater fed by the Java sea and the Flores Sea, driven by NWM currents as drawn by a previous study [32]. Also, there is a possible water mass exchange between the Banda and the Java Seas for the top 50 m [14]. While the high salinity observed in the lower mixed layer and upper thermocline layer (Figure 3b, c) in the northwestern Banda Sea, which was observed during SEM period, is likely a contribution from the intrusion of Pacific water masses flowing from the Seram Sea and the Halmahera Sea, which reaches a maximum during SEM period. Besides, the similarity of the water masses' characteristics inspected from their CFC-11 profiles in the Banda and Seram Seas depicts a possible exchange between the two basins [14]. In the core of the thermocline layer, we observed higher salinity of 34.5–34.6 psu concentrated in the central part of the trajectory, which corresponds to SEM months, while lower salinity of 34.4–34.5 psu is observed in the eastern part, which corresponds to the NWM months. These results strengthen previous studies, which concluded that the Pacific thermocline intrusion reaches its maximum during the SEM period [2], [48]–[50].

Taking 'benefit' of a relatively narrow radius of the float's trajectory, i.e., within 2°×2°, we can expose it as time-series datasets to get a general insight into hydrography temporal variability. As shown in Figure 3, seasonal variation is observed in the datasets. Temporal dynamics of the Banda Sea water masses mainly occurred in the upper 100 m layers, including the occurrence of upwelling and downwelling events as can be indicated by temperature fluctuations (Figure 3b). The observed upwelling and downwelling events correspond to the variation of the monsoonal wind affecting the region (Figure 3a, b). The upwelling season starts from the beginning of June until November (SEM) and the downwelling season starts from late November until May (NWM). We also identify an uplifting of the high salinity of 34.25–34.5 psu that reaches the near-surface layer (10 m) accompanying the upwelling events (Figure 3c). We count from March 12th to June 24th, 2018, the rate of upwelling event estimated for isotherm 27° C from 100 m to 10 m is ~0.7 m day^{-1}.

A somewhat similar seasonal upwelling and downwelling events are gained from the spatial distribution of monthly surface winds direction, surface layer transport, and vertical Ekman velocity shown in Figure 4. From January to March (see Figure 4a–c), the NWM winds induce surface layer transport toward the north direction. This is compensated by positive vertical Ekman velocity corresponding to upwelling favorable conditions in the southern area of the Banda Sea. In contrast, negative vertical Ekman velocity is associated with downwelling favorable conditions seen occupying near the Coast of Seram Island. In April, the winds start to change direction to the SEM winds (Figure 4d). During the SEM winds from May to September, surface layer transport was directed mostly southwestward (see Figure 4e–i). In May, the positive Ekman velocity corresponds to upwelling favorable events that are found across the Banda Sea (Figure 4e). The Ekman velocity then becomes stronger particularly off the coast of the north and the east region of the Banda Sea throughout June to September, followed by weak positive Ekman velocity in October. The southeasterly winds start to shift their direction to the north in November and switch to northeasterly in December.

3.2. Turbulent mixing properties

We found no seasonal difference TKE dissipation rate hence we report for the entire time period here. As shown in Figure 3e, we found a thickening pattern of high dissipation rates ($\varepsilon_{\text{Th-GM}} = 10^{-9} - 10^{-6}$ m^2 s^{-3}) layer which corresponds to the thickening of the thermocline layer during the SEM months. This relaxed/stretched thermocline layer (~less stratified) suggests a potency for the erosion of the remaining Pacific water masses signatures which entered the Banda Sea during the previous season. The dissipation rate maps in six density anomaly-based layers, representing parts of the mixed layer (σ_θ = 21–22 and 22–23), the upper thermocline/pycnocline layer (σ_θ = 23–24), the thermocline core layer (σ_θ = 24–25), the intermediate layer (σ_θ =25–26) and the deeper layer (σ_θ = 26–27) are shown in Figure 5. Table 1 shows the mean and standard deviation of dissipation rate and vertical diffusivity for certain density anomaly.

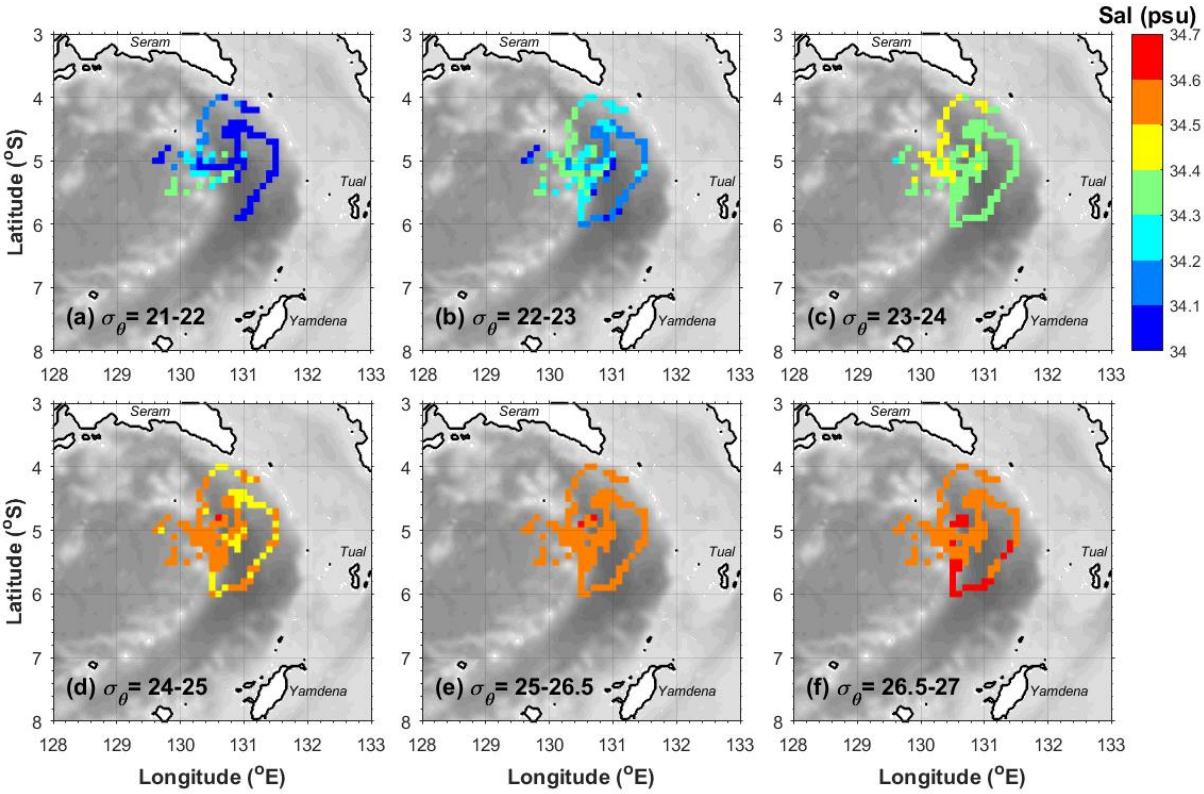

Figure 2. Horizontal distribution of 0.1° grid mean of salinity (in psu) for six selected isopycnal ranges: (a) $\sigma_{\theta\ 21\text{-}22}$, the upper mixed layer; (b) $\sigma_{\theta\ 22\text{-}23}$, the lower mixed layer; (c) $\sigma_{\theta\ 23\text{-}24}$, the upper thermocline; (c) $\sigma_{\theta\ 24\text{-}25}$, the lower thermocline; (d) $\sigma_{\theta\ 25\text{-}26.5}$ and (e) the deep layer, $\sigma_{\theta\ 26.5\text{-}27}$, which corresponds to the intermediate layer. The topography is inferred from GEBCO (General Bathymetric Chart of the Oceans).

We found that the thermocline and intermediate layers experienced higher dissipation rates of one order larger than in the deeper layer. Note that the higher dissipation rate found in the thermocline layer indicates stronger buoyancy fluxes ($\Gamma\varepsilon$) compared to the one in the upper and lower layers. Figure 3d shows a high buoyancy frequency $N > 0.01$ in the thermocline layer (σ_θ = 22–25). The high dissipation rate in the thermocline layer is consistent with the effect of stratification which focus the baroclinic energy [51]. Therefore, the stronger water mass transformation will contribute to S_{max} erosion of the Pacific thermocline. However, we remind the reader that the enhanced dissipation rates and vertical diffusivity are commonly located in the narrow passages and deeper layers which correspond to rough topography. Therefore, the largest contribution is from the shallow and narrow passages surrounding the Banda Sea, e.g. the Halmahera Straits, Lifamatola Passage, and Buru Strait [22], [25], [39]; while the contribution from the Banda Sea itself is minor. We notice that the median value of the $\varepsilon_{\text{Th-GM}}$ is one order higher than the mean value. Both indicate that the value is the thermocline layer > the mixed layer > the intermediate layer > the deep layer. Some possibilities can be responsible for the TKE dissipations in the Banda Sea. The baroclinic near-inertial waves generated by monsoonal winds may contribute to the generation of baroclinic near-inertial waves [21], [24] besides the contribution from wave-wave interactions and eddies.

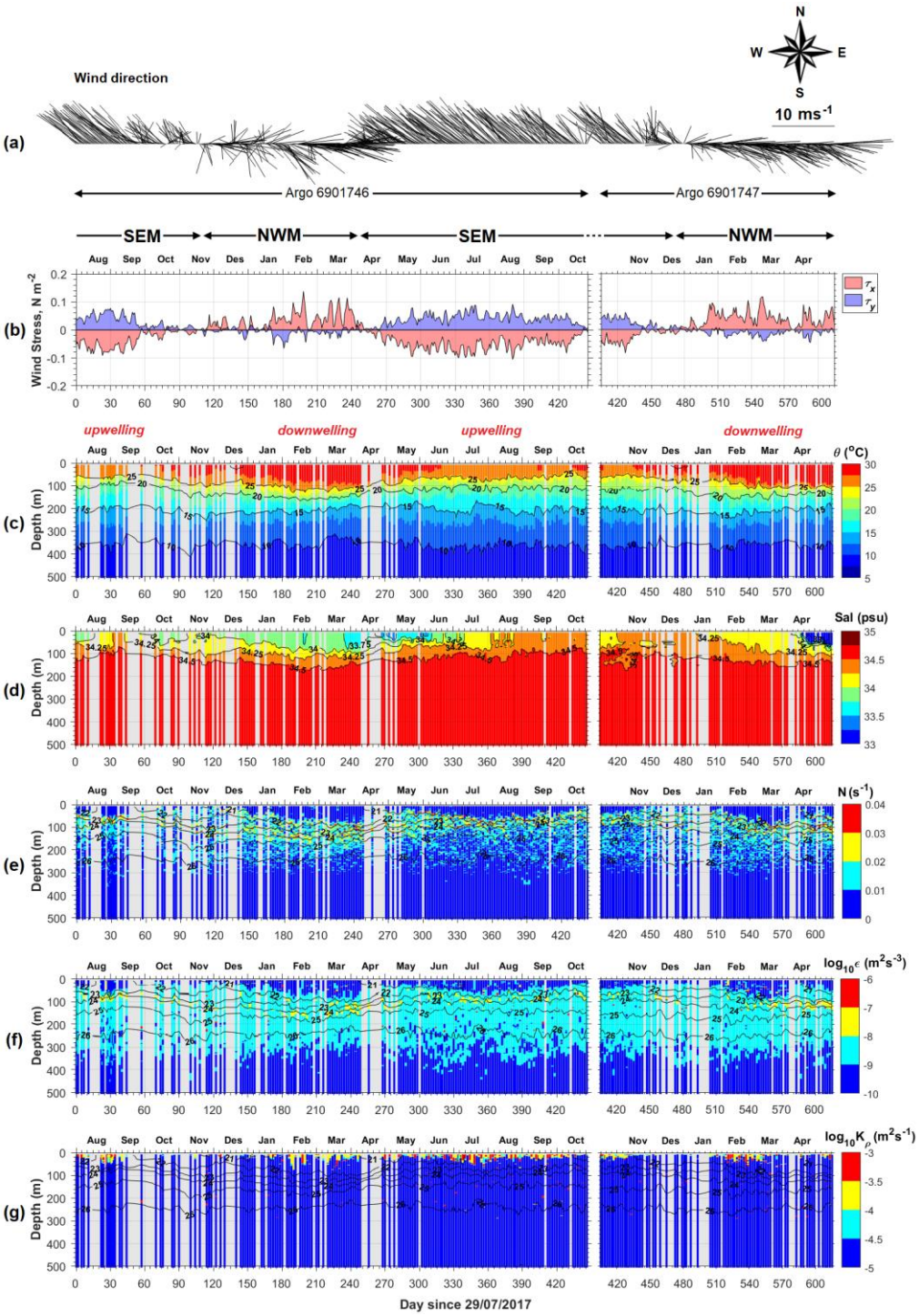

Figure 3 (a) Mean of surface winds (speed and direction) derived from the Advanced Scatterometer (ASCAT) wind data with spatial resolution of 25 km, in the region and period of Argo trajectory (129.5°–131.5° E; 4°–6° S); (b) daily means of zonal (τ_x, red) and meridional (τ_y, blue) wind stress; and time series plot of some parameters from two Argo floats (#6901746 and #6901747), shown here only for the of upper 500 m and regardless their horizontal motions within 2°×2° space: (c) temperature, (d) salinity, (e) buoyancy frequency, (f) Thorpe-based turbulent kinetic energy (TKE) dissipation rates and (g) Thorpe-based vertical eddy diffusivity. The contour lines overlaid in (e), (f), (g) are the isopycnal lines.

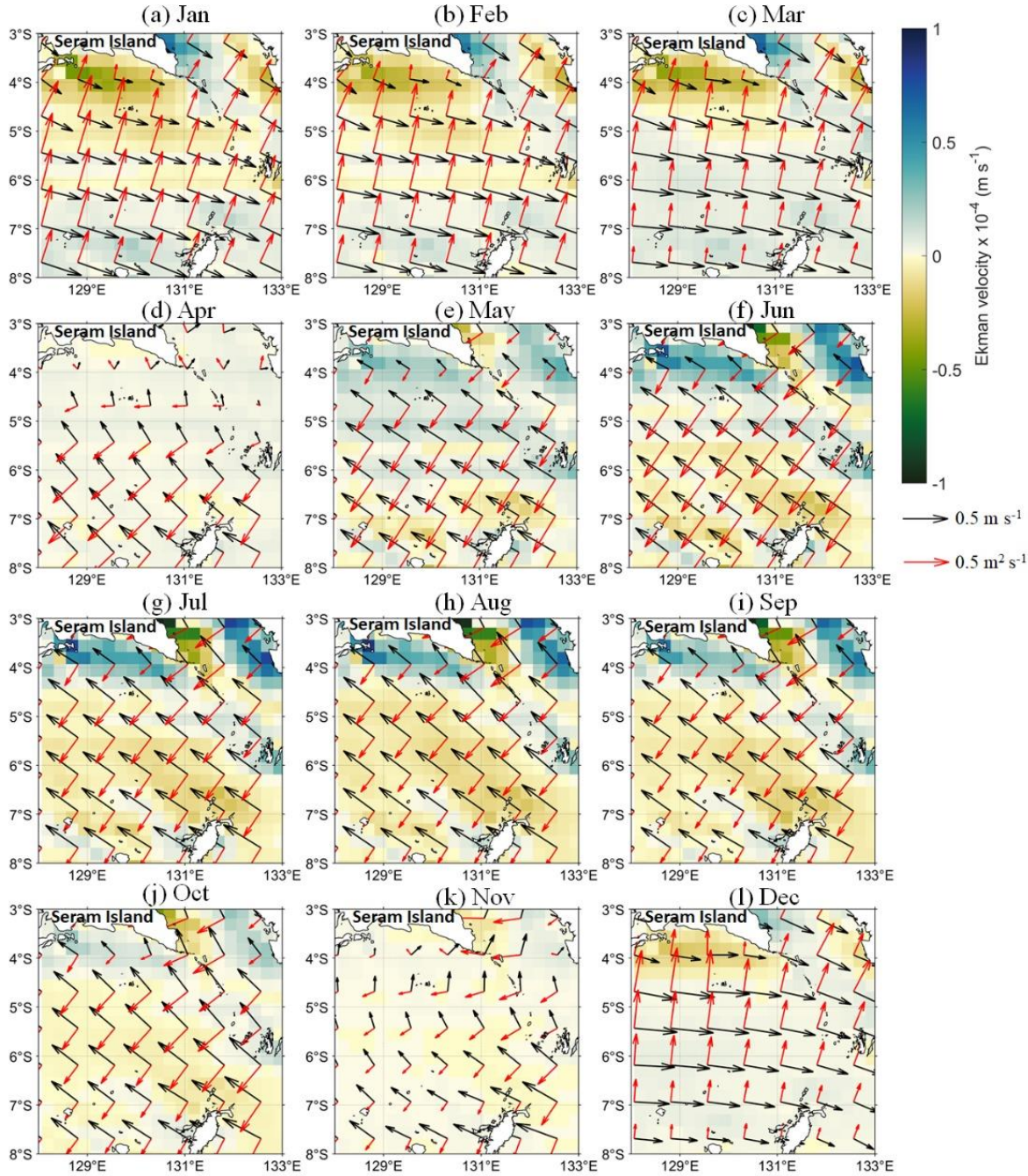

Figure 4. The mean of surface winds (black arrows) and surface layer transport (red arrows) direction averaged over the period 2017–2019 from January (a) to December (l). Blue (green) shading shows positive (negative) vertical Ekman velocity (m s^{-1}) corresponding to upwelling (downwelling) favorable conditions.

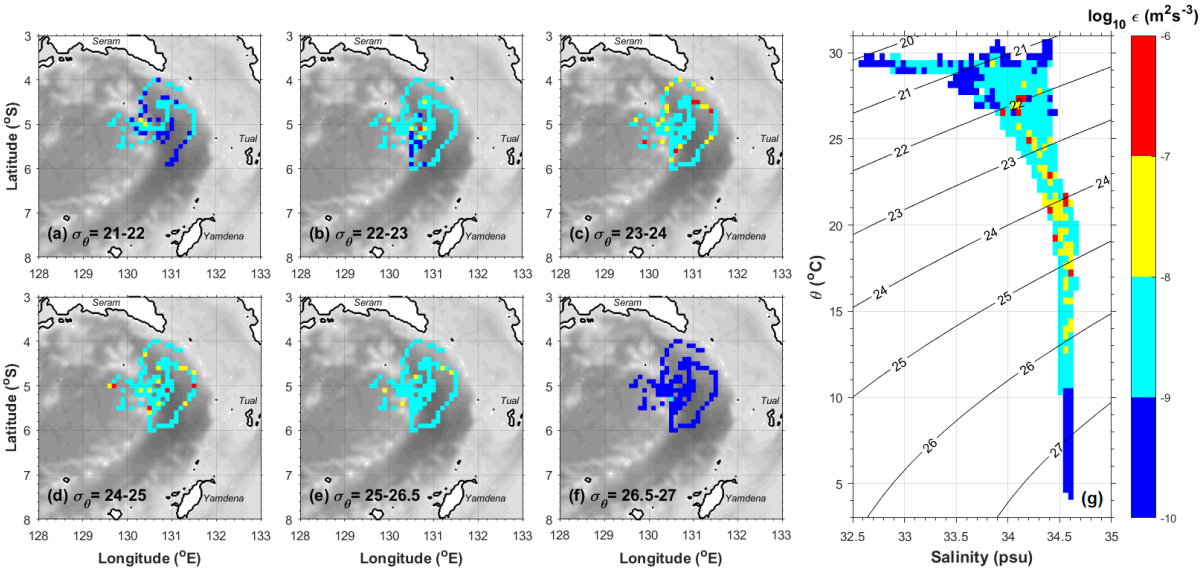

Figure 5. Horizontal map of 0.1° grid mean of the dissipation rate, $\varepsilon_{\text{Th-GM}}$ (in $\log_{10}$ scale of $m^2\ s^{-3}$) for six selected isopycnal ranges: (a) $\sigma_{\theta\ 21\text{-}22}$, the upper mixed layer; (b) $\sigma_{\theta\ 22\text{-}23}$, the lower mixed layer; (c) $\sigma_{\theta\ 23\text{-}24}$, the upper thermocline; (d) $\sigma_{\theta\ 24\text{-}25}$, the lower thermocline; (e) $\sigma_{\theta\ 25\text{-}26.5}$ the intermediate layer, (f) the deep layer, $\sigma_{\theta\ 26.5\text{-}27}$; and (g) grid averaged T/S diagram of the $\varepsilon_{\text{Th-GM}}$, in 0.4° C×0.1 psu space. The topography is inferred from GEBCO (General Bathymetric Chart of the Oceans).

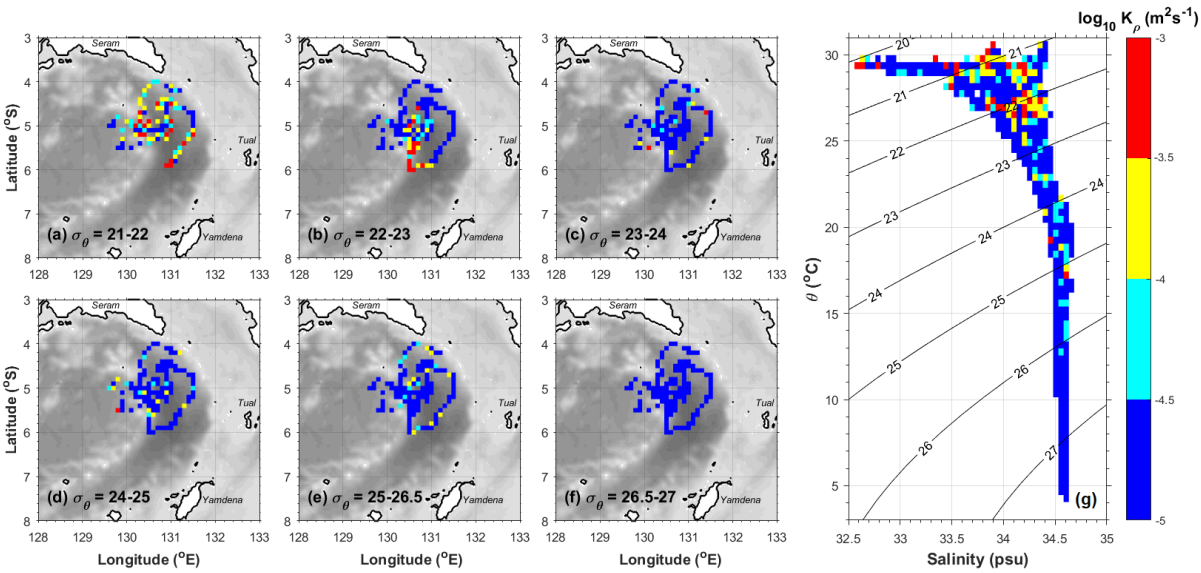

Figure 6. Horizontal map of 0.1° grid mean of the vertical diffusivity, $K_{\rho\ \text{Th-GM}}$ (in $\log_{10}$ scale of $m^2\ s^{-1}$) for six selected isopycnal ranges: (a) $\sigma_{\theta\ 21\text{-}22}$, the upper mixed layer; (b) $\sigma_{\theta\ 22\text{-}23}$, the lower mixed layer; (c) $\sigma_{\theta\ 23\text{-}24}$, the upper thermocline; (d) $\sigma_{\theta\ 24\text{-}25}$, the lower thermocline; (e) $\sigma_{\theta\ 25\text{-}26.5}$ the intermediate layer, (f) the deep layer, $\sigma_{\theta\ 26.5\text{-}27}$; and (g) grid averaged T/S diagram of the $K_{\rho\ \text{Th-GM}}$, in 0.4° C×0.1 psu space. The topography is inferred from GEBCO (General Bathymetric Chart of the Oceans).

The vertical diffusivity maps in six layers are shown in Figure 6. The higher vertical diffusivity of $K_{\rho\ \text{Th-GM}} = 10^{-4}$–$10^{-3}\ m^2\ s^{-1}$ were observed at $\sigma_\theta < 23$ kg m^{-3}. In the deeper layer ($\sigma_\theta > 23$ kg m^{-3}), the region is dominated by low diffusivity of $K_{\rho\ \text{Th-GM}} < 10^{-4}\ m^2\ s^{-1}$ with fewer spots of higher diffusivity of $K_{\rho\ \text{Th-GM}} = 10^{-4}$–$10^{-3}\ m^2\ s^{-1}$. The median value of the vertical diffusivity is the same for all layers, i.e. $4.9\times10^{-6}\ m^2\ s^{-1}$ (Table 1). A relatively low mean of vertical diffusivity obtained in the Banda Sea, i.e.

Ø10^{-4} m^2 s^{-1} in the upper layer (σ_θ = 21–23) and lower order below indicated that the Banda Sea is not the mixing hotspots as has also been suggested by previous studies [21], [22], [25], [39].

Table 1. The layer classified mean, standard deviation and median of the dissipation rate ($\varepsilon_{\text{Th-GM}}$, m^2 s^3) and vertical eddy diffusivity ($K_{\rho\ \text{Th-GM}}$, m^2 s^{-1}) for certain density anomaly range (σ_θ, kg m^{-3}).

σ_θ (kg m^{-3})	$\varepsilon_{\text{Th-GM}}$ (m^2 s^{-3})			$K_{\rho\ \text{Th-GM}}$ (m^2 s^{-1})			Note
	mean	**stdev**	**median**	**mean**	**stdev**	**median**	
21-22	8.8×10^{-9}	1.9×10^{-7}	5.3×10^{-10}	2.3×10^{-4}	9.0×10^{-4}	4.9×10^{-6}	*Mixed layer*
22-23	1.9×10^{-8}	3.0×10^{-7}	3.8×10^{-9}	1.7×10^{-4}	7.4×10^{-4}	4.9×10^{-6}	
23-24	2.5×10^{-8}	3.0×10^{-7}	7.3×10^{-9}	2.6×10^{-5}	3.3×10^{-4}	4.9×10^{-6}	*Thermocline layer*
24-25	2.5×10^{-8}	3.0×10^{-7}	4.9×10^{-9}	3.1×10^{-5}	3.6×10^{-4}	4.9×10^{-6}	
25-26.5	1.0×10^{-8}	1.8×10^{-7}	1.9×10^{-9}	2.0×10^{-5}	2.8×10^{-4}	4.9×10^{-6}	*Intermediate layer*
26.5-27	5.6×10^{-10}	2.9×10^{-10}	5.0×10^{-10}	4.8×10^{-6}	1.1×10^{-7}	4.9×10^{-6}	*Deep layer*

3.3. Comparison with direct method and models

We compare the Thorpe based estimates with direct measurements in the Banda Sea during Indonesian Mixing (INDOMIX) project in 2010 [21], [22], consisting of a single cast at 126.9980° E; 6.2855° S; and during ARLINDO Microstructure Experiment 1998 (ARMIX), consisted of 519 casts at 128° E; 6.5° S [24] using vertical microstructure profiler (hereinafter, VMP). We also compare our estimates with the output from two existing models at the same location as the INDOMIX 2010 VMP station in the Banda Sea. Since we want to see the discrepancy between the models and our Thorpe based estimates with the microstructure measurements, we focus on comparing the model profiles at the INDOMIX station which was close to the ARMIX station. Note that the float trajectory was relatively far from these microstructure stations.

We also compare the Thorpe based estimates with previous models. The NAG15 model is a 3D hydrostatic MITGCM with 1/100° resolution, forced by barotropic M_2 tides only and without background velocity. The NUG18 model is the 3D hydrostatic model NEMO 2.3 for the region of the Indonesian sea (INDESO Project) with 1/12° horizontal resolution, including atmospheric and tidal frequency of M_2, S_2, N_2, K_2, K_1, O_1, P_1, and Q_1. It is a realistic simulation, performed from January 3rd, 2007 until December 31st, 2011. This study uses the mean of the daily profile of the dissipation rate in the central Banda Sea on 11–19 July 2010 (during the INDOMIX 2010). The vertical mean profile comparison of the dissipation rate and vertical diffusivity between our Thorpe based estimates with direct measurements and models is shown in Figure 7b, c. For the Thorpe based estimates ($\varepsilon_{\text{Th-GM}}$, $K_{\rho\ \text{Th-GM}}$), the 95% confidence intervals on the mean of percentile bootstrap method [52] is shown to assess its spatiotemporal variability. Since the locations of the VMP casts differed from the area of Argo profiles trajectory, the comparison we perform here is intended to show the range of dissipation rates obtained using different methods.

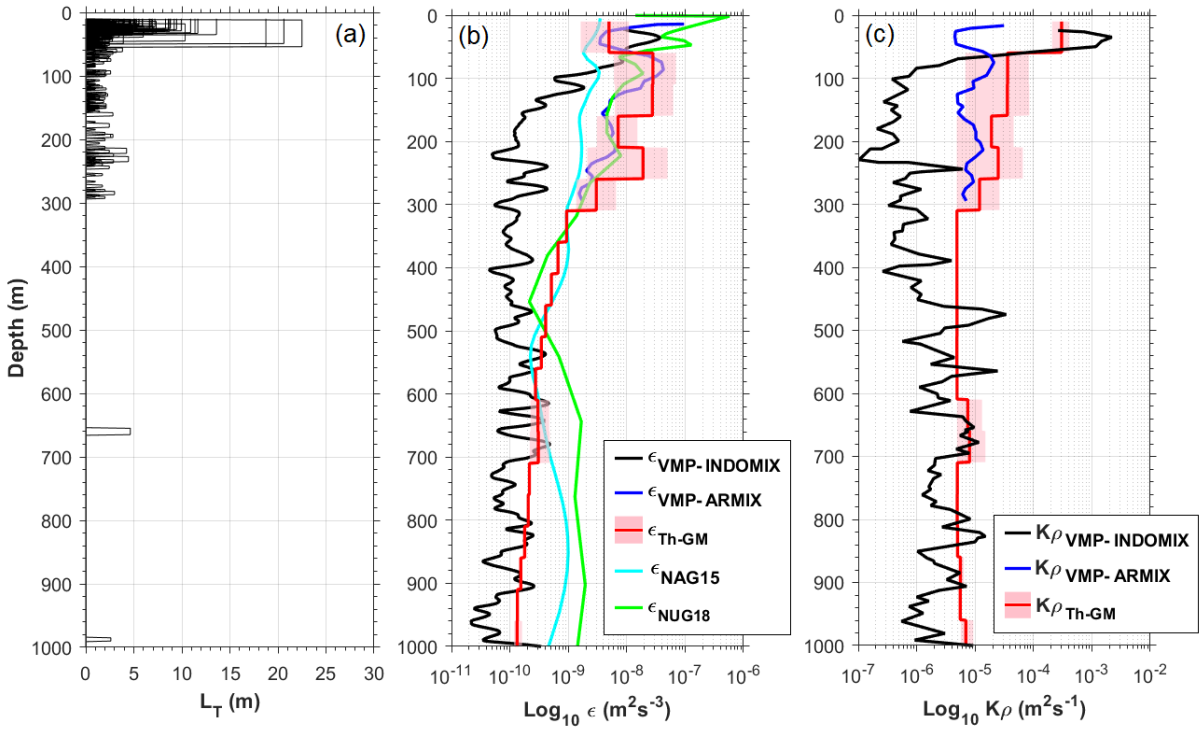

Figure 7. (a) Observed Thorpe length, L_T calculated from Thorpe displacement (d) from all Argo profiles, (b) comparison of dissipation rates mean (in $\log_{10}$, m^2 s^{-3}) from microstructure observations in the central Banda Sea (at 126.9980° E; 6.2855° S, black line, $\varepsilon_{VMP-INDOMIX}$ for INDOMIX 2010 and 128° E; 6.5° S, blue line, $\varepsilon_{VMP-ARMIX}$ for ARMIX 1999), 3D models at 126.9980° E, 6.2855° S (cyan line, ε_{NAG15} for NAG15; green line ε_{NUG18} for NUG18), and 50 m bin-averaged Thorpe estimates, ε_{Th-GM} (red); and (c) comparison of vertical diffusivity mean (in $\log_{10}$, m^{2}s^{-1}) from microstructure observations during INDOMIX 2010 (black line, $K_{\rho\ VMP-INDOMIX}$) and ARMIX 1999 (blue line, $K_{\rho\ VMP-ARMIX}$). Shading for the Thorpe estimates indicates the 95% confidence interval, denoting spatiotemporal variations within the trajectory area.

In general, for all methods, the dissipation rate is the highest in the upper 300 m layer and decreasing trend deeper. We also observed numerous turbulent overturns in the density profile, represented by the Thorpe length (L_T) in Figure 7a. In the upper 100 m layer, ε_{Th-GM} is comparable to $\varepsilon_{VMP-INDOMIX}$. Below, from 100-500 m, ε_{Th-GM} is 1–2 orders higher than the $\varepsilon_{VMP-INDOMIX}$. The ε_{Th-GM} is relatively comparable to $\varepsilon_{VMP-ARMIX}$ from 10 to 300 m. Unfortunately, there is only a single cast of VMP-INDOMIX available hence not possible to confirm temporal variation that may influence the discrepancy between $\varepsilon_{VMP-INDOMIX}$ with $\varepsilon_{VMP-ARMIX}$ and ε_{Th-GM}. We are unable to verify the tidal variation of the dissipation rates since the temporal resolution of the Argo profiles is 24 hours. Note that there can be tidal variation influencing dissipation rates magnitude as has been suggested by previous studies [21], [22], [39]. The ε_{Th-GM} is comparable to ε_{NUG18} but ~1 order higher than ε_{NAG15}. In the deeper layer below 700 m, the ε_{NAG15} overestimates the $\varepsilon_{VMP-INDOMIX}$ and ε_{Th-GM}. The ε_{NUG18} overestimates the $\varepsilon_{VMP-INDOMIX}$ below 100 m yet is well comparable to the $\varepsilon_{VMP-ARMIX}$ in the first 300 m layer. Below 500 m, the models overestimated the microstructures and our estimates. It is likely due to an overestimated background dissipation rate in the models and the coarser resolution (1/12°) of the NUG18 model hence incapable of dissipating more energy in the deeper layer.

The discrepancy between ε_{Th-GM} with $\varepsilon_{VMP-INDOMIX}$ is possible due to different background mechanisms working since they were not located at the same position and/or a limited number of VMP-INDOMIX casts hence did not cover the inertial period of the baroclinic near-inertial waves, ~3.5 days [21]. As we expected, the lower TKE dissipation rate occurred in a relatively calm area,

such as in the central Banda Sea (the INDOMIX station) while the enhanced TKE dissipation rate will occur in a more active region in the Banda Sea, such as in the Weber Deep, the area of Argo trajectory), mainly in the mixed and thermocline layers. This eastern boundary of the Banda Sea redirects currents to the south-southwest, driving a recirculation in the Banda Sea, as can be indicated in Figure 1a, and possibly generating strongly sheared currents, leading to turbulence. The discrepancy between observations and models is likely a bias that appeared in models, commonly related to the lack of a specific setup of the internal tides dissipation [26]. The constant momentum diffusion A_z set in the models seems to generate dissipation rates much larger than the observed values in the quiet region, the Banda Sea. This suggests a need for dynamical parameterization of A_z and K_z.

The mean vertical diffusivity profiles inferred from VMP and Thorpe methods are displayed in Figure 7c. Since the diffusivity estimates are sensitive to the local stratification, the discrepancy between $K_{\rho\ \text{Th-GM}}$ with $K_{\rho\ \text{VMP-INDOMIX}}$ and $K_{\rho\ \text{Th-GM}}$ is possible in this case, mainly in the thermocline layer. The VMP-INDOMIX was cast during SEM (July 2010), the VMPs-ARMIX were cast during NWM months (October-November, 1998) and Argo profiles were cast covering two periods of SEM and NWM. Stronger vertical diffusivity is observed in the upper 100 m layer, $K_{\rho\ \text{Th-GM}} > 10^{-4}$ m^2 s^{-1}, and decreasing trend deeper, $K_{\rho\ \text{Th-GM}} = 10^{-5}$–$10^{-4}$ m^2 s^{-1} in the thermocline layer [100-300] m and $K_{\rho\ \text{Th-GM}} < 10^{-5}$ m^2 s^{-1} in the deeper layer, below 300 m. Compared to $K_{\rho\ \text{VMP-INDOMIX}}$ results [21], $K_{\rho\ \text{Th-GM}}$ is comparable, mainly in the deeper layer below 300 m, i.e. between 10^{-5}–10^{-6} m^2 s^{-1}, yet slightly higher at 100–300 m layer. Interestingly, $K_{\rho\ \text{Th-GM}}$ is comparable to $K_{\rho\ \text{VMP-ARMIX}}$ if we consider a 95% confidence interval of the $K_{\rho\ \text{Th-GM}}$, suggesting a possibility of spatiotemporal variations.

4. Conclusions

Seasonal variations control water masses characteristic in the Banda Sea. The intrusion of $S_{\max}$ Pacific thermocline and $S_{\min}$ Pacific intermediate water masses were evidenced with maximum influence during the SEM months and disappeared during the NWM. The monsoonal winds system strongly drives upwelling and downwelling events, which occurred during the SEM and NWM months, respectively. The lack of direct turbulence measurements, especially in an almost unexplored area such as the Banda Sea, led us to use the indirect estimate, the Thorpe method. Compared to direct estimates, the dissipation rate and vertical diffusivity profiles gained using the Thorpe method are comparable to those observed by VMP-ARMIX except in the upper 50 m layer of the K_ρ, yet are not comparable to those observed by the VMP-INDOMIX. We also found that the semi realistic model performed comparably to our estimates and VMP-ARMIX mainly in the upper 300 m layers, while the M_2 driven estimates by the hydrostatic model seem to underestimate the values. This result underlined that local circulation of the 'trapped' Pacific water masses in the Banda Sea would be exposed to gradual/intra-seasonal mixing processes, both horizontally and vertically. We also highlighted a coupling mechanism between the upwelling event and vertical mixing which will potentially enhance nutrient enrichment in the surface layer during the SEM period, left to be explored in the future study.

Acknowledgment

This project is supported by the research scheme of *Program Riset Unggulan* COREMAP CTI 2022 (4/III/HK/2022). All authors contributed equally as the principal contributors of this manuscript.

References

[1] Gordon A L and Fine R A 1996 *Nature* **379** 6561 p. 146–149
[2] Gordon A L 2005 *Oceanography* **18** 4 p 13–13.
[3] Feng M, Zhang N, Liu Q and Wijffels S 2018 *Geosci. Lett.* **5**, 1
[4] Koch-Larrouy A, Lengaigne M, Terray P, Madec G and Masson S 2010 *Clim. Dyn.* **34**, 6 p. 891–904
[5] Wyrtki K 1961 *Sci. Resultas Mar. Investig. South China Sea Gulf Thail.* **2** p. 195
[6] Fine R A, Lukas R, Bingham F M, Warner M J and Gammon R H 1994 *J. Geophys. Res. Ocean.* **99**, C12 p. 25063–25080

[7] Bingham F M and Lukas R 1994 *J. Phys. Oceanogr.* **24** 1. p. 141–154
[8] Tsuchiya M, Lukas R, Fine R A, Firing E and Lindstrom E 1989 S *Prog. Oceanogr.* **23**, 2 p. 101–147
[9] Atmadipoera A *et al.* 2009 *Deep. Res. Part I Oceanogr. Res. Pap.* **56** 11 p. 1942–1954
[10] Kashino Y *et al.* 1996 *J. Geophys. Res. C Ocean.* **101** C5 p. 12391–12400
[11] Godfrey J S, Wilkin J and Hirst A C 1993 *J. Phys. Oceanogr* **23** 6. p. 1087–1098
[12] Li X *et al.*, 2020 *J. Phys. Oceanogr.* **50** 2 p. 471–488
[13] Van Aken H M, Punjanan J and Saimima S 1988 *Netherlands J. Sea Res.* **22** 4 p. 315–339
[14] Waworuntu J M, Fine R A, Olson D B and Gordon A L 2000 *J. Mar. Res.* **58** 4 p. 547–569
[15] Van Aken H M, Brodjonegoro I S and Jaya I 2009 *Deep. Res. Part I Oceanogr. Res. Pap.* **56** 8 p. 1203–1216
[16] Wyrtki K 1958 The water exchange between the Pacific and the Indian Oceans in relation to upwelling processes in *Proc. 9th Pacif. Sci. Congr.* **16** p. 61–66
[17] Van Bennekom A J 1988 *Netherlands J. Sea Res.* **22** 4 p. 341–354
[18] Gordon A L and Susanto R D 2001 *Ocean Dyn.* **52** 1 p. 2–10
[19] Hatayama T 2004 *J. Oceanogr.* **60** 3 p. 569–585
[20] Robertson R and Ffield A 2005 *Oceanography* **18** 4 p. 62–73
[21] Bouruet-Aubertot P *et al.* 2018 *Ocean Dyn.* **68** 7 p. 779–800
[22] Koch-Larrouy A *et al.* 2015 *Deep. Res. Part I Oceanogr. Res. Pap.* **106** p. 136–153
[23] Alford M H and Gregg M C 2001 *J. Geophys. Res.* **106** C8 p. 16947–16968
[24] Alford M H, Gregg M C and Ilyas M 1999 *Geophys. Res. Lett.* **26** 17 p. 2741–2744
[25] Nagai T and Hibiya T 2015 *J. Geophys. Res. Ocean.* **120** 5 p. 3373–3390
[26] Nugroho D, Koch-Larrouy A, Gaspar P, Lyard F, Reffray G and Tranchant B 2018 *Mar. Pollut. Bull.* **131** June p. 7–18
[27] Nagai T, Hibiya T and Bouruet-Aubertot P 2017 *J. Geophys. Res. Ocean.* **122** 11 p. 8933–8943
[28] Argo data selection. [Online]. Available: http://www.argodatamgt.org/Access-to-data/Argo-data-selection
[29] Argo Data Management Team, 2019 *Argo user's manual* Argo Data Management.
[30] Remote sensing systems. [Online]. Available: https://www.remss.com/
[31] Gordon A L 2001 Chapter 4.7 Interocean exchange, in *Ocean Circulation and Climate*, **77**, G. Siedler, J. Church, and J. B. T.-I. G. Gould, Eds. (Academic Press), p. 303–314
[32] Gordon A L and McClean J L 1999 *J. Phys. Oceanogr.* **29** p. 198–216
[33] Kunze E, Firing E, Hummon J M, Chereskin T K and Thurnherr A M 2006 *J. Phys. Oceanogr.* **36** 8 p. 1553–1576
[34] Whalen C B, Talley L D and MacKinnon J A 2012 *Geophys. Res. Lett.* **39** 17 p. 1–6
[35] Kunze E 2017 *J. Phys. Oceanogr.* **47** p. 1325–1345
[36] Park Y H, Lee J H, Durand I and Hong C S 2014 *Biogeosciences* **11** 23 p. 6927–6937
[37] Ferron B, Mercier H, Speer K, Gargett A and Polzin K 1998 *J. Phys. Oceanogr.* **28** 10 p. 1929–1945
[38] Yang Q, Zhao W, Li M and Tian J 2014 S *J. Phys. Oceanogr.* **44** 8 p. 2235–2247
[39] Purwandana A, Cuypers Y, Bouruet-Aubertot P, Nagai T, Hibiya T and Atmadipoera A S 2020 *Prog. Oceanogr.* **184** March p. 102312
[40] Garrett C and Munk W 1975 *J. Geophys. Res.* **80** 3 p. 291–297
[41] Osborn T R 1980 *J. Phys. Oceanogr.* **10** 1. p. 83–89
[42] Enriquez A G and Friehe C A 1995 *J. Phys. Oceanogr.* **25** 7. p. 1651–1671
[43] Azis Ismail M F, Ribbe J, Karstensen J, Lemckert C, Lee S and Gustafson J 2017 *Estuar. Coast. Shelf Sci.* **192** p. 72–85
[44] Greene C A *et al.* 2019 *Geochemistry, Geophys. Geosystems* **20** 7 p. 3774–3781
[45] Ollitrault M and Rannou J-P 2013 *J. Atmos. Ocean. Technol.* **30** 4 p. 759–788
[46] Liang L, Xue H and Shu Y 2019 *J. Geophys. Res. Ocean.* **124** 5 p. 3089–3106
[47] Zhu Y *et al.* 2019 *J. Geophys. Res. Ocean.* **124** 10 p. 7030–7045

[48] Sprintall J, Wijffels S E, Molcard R and Jaya I 2009 *J. Geophys. Res. Ocean.* **114** 7 p. 1–19
[49] Moore T S, Marra J and Alkatiri A 2003 *Mar. Ecol. Prog. Ser.* **261** 1997 p. 41–49
[50] Bayhaqi A *et al.* 2019 *Am. J. Appl. Sci.* **16** 4 p. 118–133
[51] Cuypers Y, Bouruet-Aubertot P, Vialard J and McPhaden M J 2017 *Geophys. Res. Lett.* **44** 5 p. 2398–2406
[52] Efron B and Tibshirani R J 1994 *An Introduction to the Bootstrap* Chapman & Hall CRC